Q. J. R. Meteorol. Soc. (2003), **129**, pp. 693–713 doi: 10.1256/qj.02.39

A comparison of ground-based Doppler lidar and airborne *in situ* wind observations above complex terrain

By DALE R. DURRAN[1]*, TOMISLAV MARIC[1], ROBERT M. BANTA[2], LISA S. DARBY[2] and R. MICHAEL HARDESTY[2]

[1]*University of Washington, Seattle, USA*
[2]*Environmental Technology Laboratory, NOAA, Boulder, USA*

(Received 31 January 2002; revised 27 July 2002)

SUMMARY

Airborne wind observations collected by the National Oceanic and Atmospheric Administration's (NOAA) WP-3D aircraft are compared with the winds retrieved by the NOAA/Environmental Technology Laboratory's ground-based scanning Doppler lidar within the Wipp Valley during the Special Observing Period of the Mesoscale Alpine Programme. Comparisons are performed along individual flight tracks and over an aggregated dataset consisting of all pairs of WP-3D and lidar observations that were approximately coincident in time and space. The impact of several different quality-control thresholds on the root mean square (r.m.s.) difference between the two observations is explored. The overall quality-controlled r.m.s. difference between radial wind speeds measured by each platform was 3.0 m s^{-1}, with larger r.m.s. errors in the region up valley from the lidar than in the region down valley. A bias was also evident, in which the wind speeds from the WP-3D exceeded those from the lidar; this bias was small down valley (0.4 m s^{-1}) and much larger up valley (2.4 m s^{-1}).

KEYWORDS: Gap flow Mesoscale Alpine Programme Wind measurement

1. INTRODUCTION

Detailed and extensive measurements of the airflow within the Wipp Valley (hereafter the Wipptal) south of Innsbruck, Austria were obtained during the intensive field phase of the Mesoscale Alpine Programme (MAP) in the fall of 1999 (Bougeault *et al.* 2001). Two particularly significant instrument platforms used to gather these observations were a ground-based scanning Doppler lidar operated by the Environmental Technology Laboratory (ETL) of the National Oceanic and Atmospheric Administration (NOAA) within the valley at Gedeir, and the NOAA WP-3D (hereafter the P-3), which collected a full suite of *in situ* meteorological data along flight legs parallel to the axis of the valley. Composite analyses of the flow in the Wipptal using both the Doppler lidar and the P-3 have been performed (e.g. Flamant *et al.* 2002) and more are in progress. The validity of these analyses depends critically on the reliability and consistency of the wind values obtained from each instrument. In this paper we present a detailed comparison of the wind-speed observations collected by these two systems on those days when the P-3 flew through regions that were almost simultaneously scanned by the Doppler lidar.

The precision of the velocity measurements for the Doppler-lidar used in MAP was previously determined to be 0.6 m s^{-1} using a hard-target calibration (Post and Cupp 1990). Doppler-lidar determinations of the vertical profile of the horizontal wind computed from full 360° conical scans have also been compared with coincident rawinsonde releases by Hall *et al.* (1984), who found that the measurements differed by 1.5 m s^{-1} root mean square (r.m.s.) for wind speed and 15° r.m.s. for direction. Hall *et al.* (1984) also presented comparisons between lidar winds, again computed from 360° conical scans, and anemometer measurements from a 300 m high tower which showed r.m.s. differences of 0.34 m s^{-1}, although the r.m.s. differences for each of the raw lidar wind datum points varied between 1.07 m s^{-1} and 2.57 m s^{-1}. Comparisons between Doppler lidars and other instrument platforms with the goal of evaluating each

* Corresponding author: Department of Atmospheric Sciences, Box 351640, University of Washington, Seattle, WA 98195, USA. e-mail: durrand@atmos.washington.edu

instrument in non-steady, non-homogeneous atmospheric conditions, such as airflow over topography, have been hard to obtain. Such comparisons are especially difficult at levels well above the ground, since they require near-simultaneous observations of nearly the same point in the atmosphere. The gap-flow experiment in MAP has provided an unprecedented opportunity to compare wind data from two very different measuring systems, the Doppler lidar and the P-3, in mesoscale airflow over complex terrain.

2. The data sources

(*a*) *The NOAA P-3 observations*

The horizontal wind speed is determined as the difference between the horizontal components of the true air speed of the P-3 and the ground-relative velocity of the aircraft. The ground-relative velocity is obtained from one of a pair of inertial navigation systems (INS). The decomposition of the true air speed into orthogonal components is computed from the roll, pitch, and heading (determined from the INS) and from the angle of attack and side-slip (determined from differential pressure transducers). The true air speed is computed from static and dynamic pressure sensors in pitot ports on the wing and fuselage after correction for variations in atmospheric density and temperature. The vertical wind speed is determined by the difference between the vertical component of the true air speed and integrated vertical accelerometer data blended with the rate of change of selected data from the radar altimeter.

The horizontal position of the P-3 is determined primarily from the INS with some correction from the on-board military-grade (P code) Global Positioning System (GPS). The GPS position is not used as the primary reference because satellite coverage is not always adequate, the GPS signal may be lost in steep turns (in which the roll angle exceeds 25°) due to the antenna placement and the GPS output (at 1 HZ) is 40 times slower than the output from the INS (at 40 Hz). The vertical position of the P-3 was determined by the pressure altitude. The uncertainty in the P-3 position data is roughly 100 m in the horizontal and 10 m in the vertical (A. Barry Damiano, personal communication).

Further details about the NOAA P-3 may be obtained from NOAA's Aircraft Operations Center website at http://www.hurricanehunters.noaa.gov/, June 2002. The final quality-controlled data are used in this comparison; these data may be downloaded from ftp://map.ethz.ch/fgop5/data/flights/p-3/p3fltlvldata/, December 2001.

(*b*) *The NOAA/ETL scanning Doppler lidar*

Doppler lidar is an active-remote-sensing, wind-measuring instrument. The lidar deployed during MAP, which we refer to as TEACO2 because of its configuration (Transverse-Excited Atmospheric pressure discharge laser, or TEA laser) and because it uses carbon dioxide (CO_2) laser technology, is described by Post and Cupp (1990). It transmits a pulse of eye-safe, coherent infrared light, which scatters off aerosol particles; a small fraction of the transmitted radiation is subsequently detected back at the lidar. For typical atmospheric aerosol size distributions, most of the backscattered radiation comes from particles about 1 μm in diameter (Post 1978; Banta *et al.* 1992). Particles of this size are excellent tracers of atmospheric motion. This lidar has been used in several studies of flow in complex terrain, including the Grand Canyon (Banta *et al.* 1999).

For a detailed discussion of the technical characteristics and some of the history of the development of the TEACO2 Doppler lidar the reader is referred to Post and Cupp (1990). Several of the characteristics relevant to this study are given in Table 1.

TABLE 1. CHARACTERISTICS OF THE TEACO2 DOPPLER LIDAR DURING MAP

Wavelength (μm)	10.59
Maximum range (km)	Up to 30
Minimum range (km)	1.2
Range resolution (km)	0.3
Beam divergence (°)	0.005
Data sampling frequency (MHz)	15
r.m.s. velocity precision (m s^{-1})	0.6
Pulse repetition frequency (Hz)	10
Pulses averaged per beam	3
Effective pulse rate (Hz)	3.33
Standard scan rate (° s^{-1})	3.33
Angular resolution (°)	1.0

Of interest here is that the data from individual lidar shots are taken in range bins or gates at 300 m intervals at a pulse repetition frequency of 10 Hz. Data are then averaged across three shots into a 'beam' to reduce noise and improve the reliability of the velocity estimates. The minimum range of the lidar, which is dictated by the hardware, is 1.2 km. The maximum range depends on the signal-to-noise ratio (SNR) which compares the detected signal power from a particular range to the mean noise power level in the receiver. The signal strength is a function of both lidar system parameters (such as laser pulse energy, transceiver telescope aperture area, optical system losses, target range) and atmospheric conditions (beam attenuation, backscatter cross-section, optical turbulence). At this wavelength, attenuation is generally dominated by water-vapour and carbon-dioxide absorption, although there may also be a significant contribution from scattering by aerosol particles.

Velocity estimates are obtained by measuring the Doppler shift in the frequency of the backscattered signal. The accuracy of a velocity estimate depends on that of the frequency estimate. Frequency is one of the most reliable remotely measured quantities. The precision of the frequency estimate in optical lidar depends primarily on the effective photo count in the received signal, which can be shown to be the product of the SNR, the number of discrete data points sampled in a range gate, and the number of pulse returns averaged.

To compute the mean frequency of the return, a 'poly-pulse pair' algorithm is applied (Rye and Hardesty 1993). In very broad terms, the algorithm is summarized as follows. The return from each pulse is passed through an analogue complex demodulator and the output from each demodulator channel is digitized at 15 MHz. In software, the return is segmented into range gates, for each of which an autocovariance function (ACF) is formed and averaged over the three returns. The ACF is truncated to a small number of lags (fewer than six) so that use of a fast Fourier transform (FFT) routine results in a somewhat smoothed power spectrum. The mean of the backscattered return is computed from a Gaussian fit to the spectral peak in the computed power spectrum. This algorithm, which is easily implemented, has been shown to provide performance approaching that of a maximum likelihood estimator (Rye and Hardesty 1993). Confidence in the frequency estimate is characterized by two quality-control parameters that are readily derived from these products. First, backscattered signal intensity B, which is proportional to the height of the spectral peak above the system noise, is an indicator of the sample SNR within a narrow frequency band around the signal. The second parameter, the 'signal quality index' S_{QI}, which is the ratio of the amplitudes of the first and zeroth lag of the ACF, is an indicator of the power in the correlated or signal-dependent component of the return relative to the total power (noise

plus signal). Although the S_{QI}, as defined above, is always less than 1, it is quoted as an integer essentially after multiplication by 255.

Pulsed TEA laser transmitters of the type employed in the NOAA TEACO2 system are typically characterized by pulse-to-pulse frequency jitter as well as sweeping of the absolute frequency within the period of the pulse (i.e. frequency 'chirp'). Chirp, which is caused by changes in the temperature and hence the refractive index of the laser gas, broadens the bandwidth of the return, and can lead to biases in the wind estimate if not taken into account in the signal processing. In the NOAA system, effects of frequency jitter and chirp are minimized by sampling each laser pulse as it is transmitted, and then computing its mean frequency (relative to the local oscillator laser reference). This estimated laser-pulse frequency is then subtracted from the frequency estimate of the backscattered signal.

TEACO2 scans in azimuth and elevation. For this study, we focus on the scans that produced a three-dimensional (3D) volume of data either pointing up valley toward the Brenner Pass (at approximately 178° azimuth), or down valley toward Innsbruck (at approximately 320° azimuth). This was accomplished in two ways, using either azimuth or elevation scans. The procedure for azimuth scanning was to perform a horizontal sector scan at 0° elevation, to move up 1° in elevation and repeat the sector scan at the new elevation, and to continue this process until the highest-elevation scan was completed, thus covering the 3D volume. The azimuthal sector scans increased from 0° to 20° elevation in steps of 1°. For elevation scanning the procedure was similar, except that the elevation sector scans were vertical slices from 0° to 30° elevation, collected at 1.5° increments in azimuth angle.

3. The comparison methodology

The topography surrounding the Wipptal is shown in Fig. 1, together with the position of the lidar, the average flight track of the P-3 between 1038 and 1322 UTC on 20 October 1999, and the horizontal footprint of typical lidar volume scans directed up valley (to the south of the lidar) and down valley (to the north-west). Roughly 6 minutes were required to complete each Doppler-lidar volume scan, whereas the P-3, travelling at an air speed of between 100 and 120 m s^{-1}, typically passed through that volume in less than two minutes. Let t_L denote the middle of the time interval during which a lidar volume scan was collected, and define t_{P3} as the time at which the P-3 was at the midpoint of its trajectory through the volume sampled by the lidar. There were a total of 24 flight legs on three different days in which the P-3 passed through a volume being scanned by the Doppler lidar and the two observations were sufficiently close to simultaneous that $|t_L - t_{P3}| \leqslant 10$ minutes. These flight legs are listed in Table 2, together with the characteristics of the associated lidar volume scan. Note that in several cases there are actually two P-3 flights that meet the time-selection criteria for the same lidar volume scan.

Point-by-point comparisons between the lidar and P-3 wind data were created as follows. Each beam of three lidar pulses samples a 300 m long cylinder of air extending outward along a radial line from the transceiver. The cylinder itself is very narrow, only about 1 metre in diameter, 11 km down range of the lidar. The return from each beam was assumed to be representative of the radial wind at the centroid of each 300 m long cylinder. The eight centroids containing each P-3 observation in the smallest possible parallelepiped were identified and used to linearly interpolate the lidar data to the same spatial location as the P-3 observation.

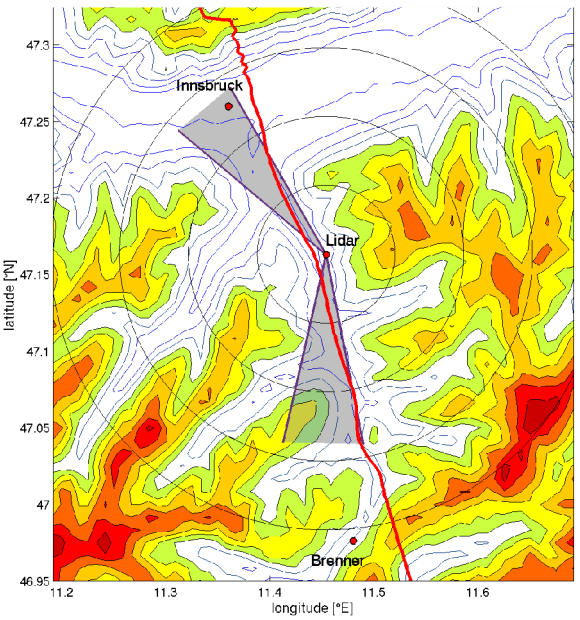

Figure 1. Topography of the Wipptal showing the average track of the P-3 on 20 October 1999 (red line) and two lidar volume scans. Terrain contours are plotted at 250 m intervals, elevations greater than 1750 m are colour filled.

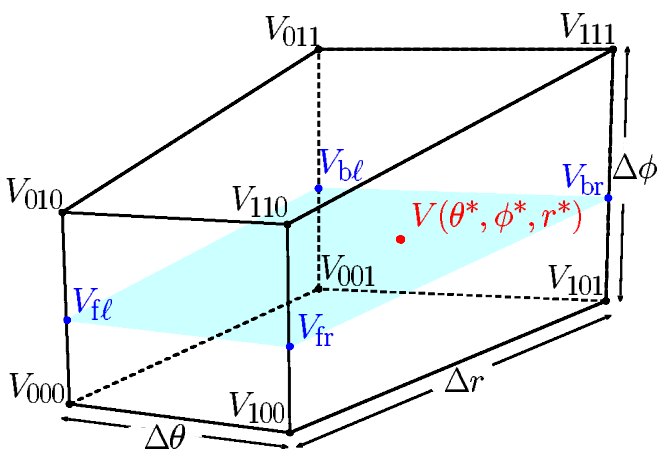

Figure 2. Polyhedron formed by the data at eight lidar centroids ($V_{000}, V_{100}, \ldots$) surrounding the point (θ^*, ϕ^*, r^*) at which the P-3 observation was collected. Also shown are the locations of $V_{f\ell}$, $V_{fr}, \ldots$ in the $\phi = \phi^*$ surface to which the centroids are first interpolated. The face containing $V_{000}V_{010}V_{110}V_{100}$ is closest to the lidar.

In fact, the polyhedron defined by the vertices of the lidar centroids is generally not a perfect parallelepiped and this was accounted for by the interpolation algorithm. The lidar volume scans were constructed from either a series of azimuthal scans (scans at constant elevation angle ϕ) or a series of elevation scans (scans at constant azimuth angle θ). Without loss of generality we consider the case where the volume was constructed from elevation scans. This situation is shown in Fig. 2, in which eight lidar centroids surround a P-3 observation at point (θ^*, ϕ^*, r^*), where θ^*, ϕ^*, and r^* are, respectively,

TABLE 2. LIDAR VOLUME SCANS WHICH APPROXIMATELY COINCIDE WITH P-3 FLIGHT LEGS

Lidar volume scan		P-3 flight leg(s)		
Time	Type	Time	Altitude (m above mean sea level)	Time Difference
		20 October 1999		
1100:42–1106:01	A, D	1054:40–1055:45	1720	8:09
		1109:30–1110:45	1470	−6:46
1253:44–1259:02	A, D	1251:05–1252:40	2000	4:30
		1304:20–1305:15	1560	−8:25
1314:03–1319:07	A, D	1309:20–1310:40	2640	6:35
		1321:05–1323:00	1230	−5:27
		30 October 1999		
0953:21–0958:24	A, U	0948:10–0950:20	2080	6:37
		0957:00–1000:10	2370	−2:43
1012:27–1019:36	E, U	1014:30–1017:00	1900	0:17
		1022:30–1024:45	1620	−7:36
1054:25–1059:41	A, D	1051:00–1052:15	2690	5:26
		1104:50–1106:05	1030	−8:25
1114:10–1120:45	E, D	1110:40–1112:15	1330	6:00
		1124:05–1126:30	1250	−7:50
1310:22–1315:37	A, D	1319:25–1320:50	3610	−7:08
1328:41–1335:15	E, D	1334:15–1335:45	2100	−3:02
1423:19–1428:23	A, U	1424:10–1426:40	2720	0:26
1442:12–1449:24	E, U	1434:20–1435:20	1370	9:02
		1444:30–1447:00	3030	0:03
1532:37–1537:52	A, D	1536:15–1539:00	2090	−2:23
		1540:00–1542:25	2270	−5:58
1555:37–1602:11	E, D	1554:30–1556:05	1480	5:58
		11 November 1999		
1358:54–1404:11	A-D	1355:46–1357:15	1120	5:02
		1400:40–1402:30	2350	−0:03

The time interval over which each volume scan was collected is given in the first column; volumes constructed from successive azimuthal (elevation) scans are denoted by A (E); up-valley and down-valley scans are denoted by U or D respectively. The times for the P-3 flight legs are the periods during which the plane occupied the volume scanned by the lidar. The P-3 altitude varies along each leg; the figure given is representative of the down-valley portion of the leg. The time difference is $t_L - t_{P3}$ (see text) in minutes and seconds.

the azimuth angle, elevation angle, and radial distance with respect to a spherical coordinate system whose origin coincides with the lidar transceiver. When the volume is constructed from adjacent elevation scans, the elevation angles of corresponding points on the 'right' and 'left' faces of the polyhedron are not necessarily identical. The data on the left face and the data on the right face are, therefore, separately interpolated to the surface $\phi = \phi^*$ as follows. Let $\beta_\ell = (\phi^* - \phi_{\ell_0})/\Delta\phi_\ell$ and $\beta_r = (\phi^* - \phi_{r_0})/\Delta\phi_r$, where $\Delta\phi_\ell$ and $\Delta\phi_r$ are the changes in elevation angle (in radians) between the top and bottom of the left and right sides of the box in Fig. 2; ϕ_{ℓ_0} is the elevation angle of centroid 000 (and 001), and ϕ_{r_0} is the elevation angle of centroid 100 (and 101).

Wind speeds at four points on the $\phi = \phi^*$ surface are then computed from the relations

$$V_{f\ell} = (1 - \beta_\ell)V_{000} + \beta_\ell V_{010}, \tag{1}$$

$$V_{b\ell} = (1 - \beta_\ell)V_{001} + \beta_\ell V_{011}, \tag{2}$$

$$V_{fr} = (1 - \beta_r)V_{100} + \beta_r V_{110}, \tag{3}$$

$$V_{br} = (1 - \beta_r)V_{101} + \beta_r V_{111}. \tag{4}$$

To complete the calculation let $\alpha = (\theta^* - \theta_0)/\Delta\theta$ and $\gamma = (r^* - r_0)/\Delta r$, where θ_0 and r_0 are the azimuth angle and the radial coordinate of the centroid 000. Then the

interpolated radial wind speed at the location of the P-3 observation is

$$S(\theta^*, \phi^*, r^*) = (1-\alpha)\{(1-\gamma)V_{f\ell} + \gamma V_{b\ell}\} + \alpha\{(1-\gamma)V_{fr} + \gamma V_{br}\}. \quad (5)$$

The same formulae, Eqs. (1)–(5), are also used to interpolate the times at which the lidar data were collected at each of the eight centroids and thereby assign a time t_L^* to the linearly interpolated radial wind speed $V(\theta^*, \phi^*, r^*)$. Other quality-control parameters, such as the backscatter and the signal quality index were interpolated in the same manner to yield values representative of the signal quality at point (θ^*, ϕ^*, r^*).

A similar algorithm is executed for those volumes composed of successive azimuthal scans, except that the data are first interpolated to a surface of constant azimuth angle, rather than a surface of constant elevation angle. When the volume is composed of successive azimuthal scans the increment in elevation angle ($\Delta\phi$) is 1.0 degrees and the increment in azimuth angle ($\Delta\theta$) is approximately 1.05 degrees. In contrast, when the volume is composed of successive elevation scans, $\Delta\theta$ is 1.5 degrees and $\Delta\phi$ is approximately 0.55 degrees. In both cases Δr is 300 m.

The tri-linear interpolation used to compute $V(\theta^*, \phi^*, r^*)$ introduces some modest smoothing in the point-wise estimates obtained from the lidar data. The P-3 wind data were, therefore, slightly smoothed by applying the three-point filters

$$\tilde{u}_i = (u_{i-1} + 2u_i + u_{i+1})/4, \qquad \tilde{v}_i = (v_{i-1} + 2v_i + v_{i+1})/4, \quad (6)$$

to the values for each horizontal wind component, where $i-1$ and $i+1$ denote the P-3 wind observations taken immediately prior to and after the observation at point i, and the tilde denotes a filtered value.

4. Results

We begin by considering detailed comparisons of the data gathered along four individual flight legs, and then we present an integrated look at the complete dataset.

(*a*) *Comparisons along individual flight legs*

The first comparison involves the P-3 leg on 20 October 1999 between 1251:05 and 1252:40 UTC when the aircraft was flying at approximately 2000 m (all heights quoted are above mean sea level) near the mouth of the Wipptal about 4 minutes before the lidar scanned the same area. The lidar-retrieved radial wind field at 1980 m is shown by the colour-filled contours in the right and left sections of Fig. 3. The topography is indicated by the background grey-scale shading such that darker greys represent lower elevations, with a contour interval of 250 m. The intersections of latitude and longitude lines, at 5-minute intervals, are indicated by cross-hairs. The north–south and east–west distances between adjacent cross-hairs are, therefore, 9.25 and 6.28 km, respectively.

The P-3 flight track is shown in each section of Fig. 3 by a pair of heavy black lines. In the left section, the colour fill between this pair of lines indicates the P-3's elevation along the flight track. Note that the P-3 flight track is almost perfectly level and only 20–40 m above the level to which the lidar volume scan data were interpolated. The colour fill within the track on the right section shows the horizontal wind component along the line between the P-3 and the lidar as computed from the horizontal winds observed by the P-3. When there is perfect agreement between the two observations, the colour is identical inside and outside the pair of heavy lines. The total horizontal wind vector is also plotted, along with the value of the total horizontal wind speed, every 15 seconds along the P-3 flight track in the right section of Fig. 3. The images

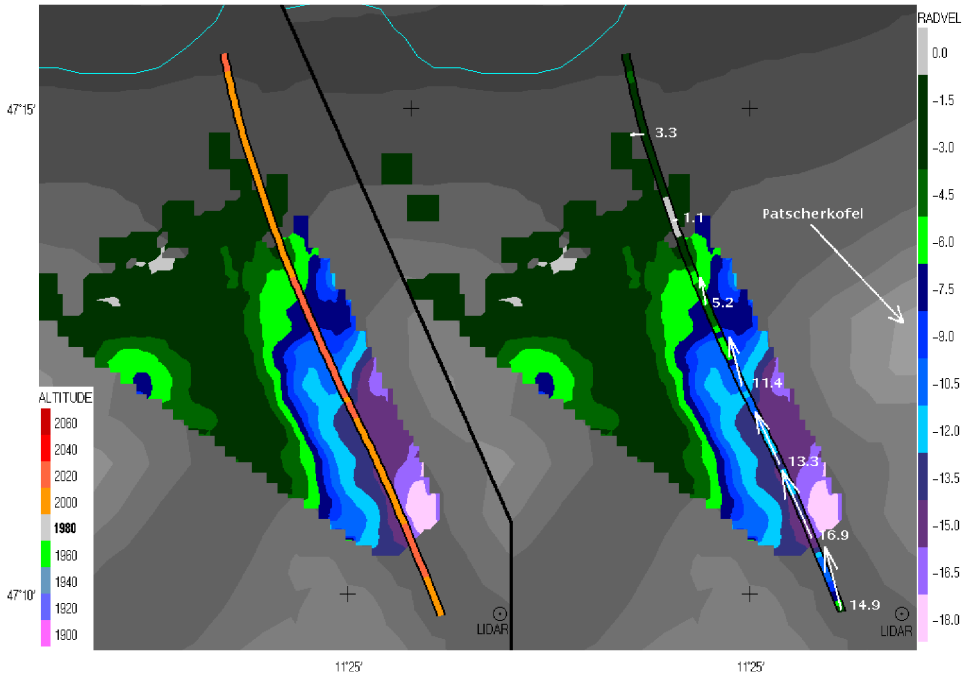

Figure 3. Comparison of P-3 and lidar radial wind data at approximately 1252 UTC on 20 October 1999. The lidar-retrieved radial wind speed (m s^{-1}) interpolated to a horizontal plane at 1980 m (above mean sea level) is indicated in each section by the colour-filled contours. The surface topography is indicated by the background grey scale. The left section shows altitude variations (m) of the P-3 along the flight track. The right section shows the radial wind component observed by the P-3 using the same colour scale as for the lidar data itself. Total horizontal wind vectors and wind speeds are shown by the white vectors and numbers at 15 second intervals along the track. See text for further details.

shown in Fig. 3 were obtained using the MountainZebra software package (James *et al.* 2000) which was designed for the simultaneous display of radar, aircraft, and other data in mountainous terrain. MountainZebra is an extension of the Zeb software package (Corbet *et al.* 1994) developed by the Atmospheric Technology Division of the National Center for Atmospheric Research.

The agreement between the two datasets shown in the right section of Fig. 3 is rather good, although the winds observed by the P-3 do decrease somewhat more rapidly down valley than those recorded by the lidar. Also evident in the contoured lidar data is the tendency for the radial winds to be significantly stronger on the east side of the Wipptal along the flank of Patscherkofel mountain. At least along the east side of the Wipptal the total horizontal wind vector is clearly directed down valley and the distribution of the total wind speed appears to be reasonably well approximated by the field of the radial wind speed.

A more quantitative comparison along the same flight track is provided in Fig. 4, in which the three-dimensional wind velocity observed at 1 s intervals by the P-3 is projected onto the radial line between the P-3 and the lidar, and plotted as a function of *radial* distance downstream from the lidar using solid coloured circles. The P-3 data are smoothed along the flight track using the three-point filter Eq. (6). The lidar-derived winds are linearly interpolated to the point at which the P-3 data were collected using the algorithm described in section 3. The lidar data appearing in Fig. 4 (and subsequently in Figs. 6, 8 and 10) satisfy the quality-control condition that the variance among the

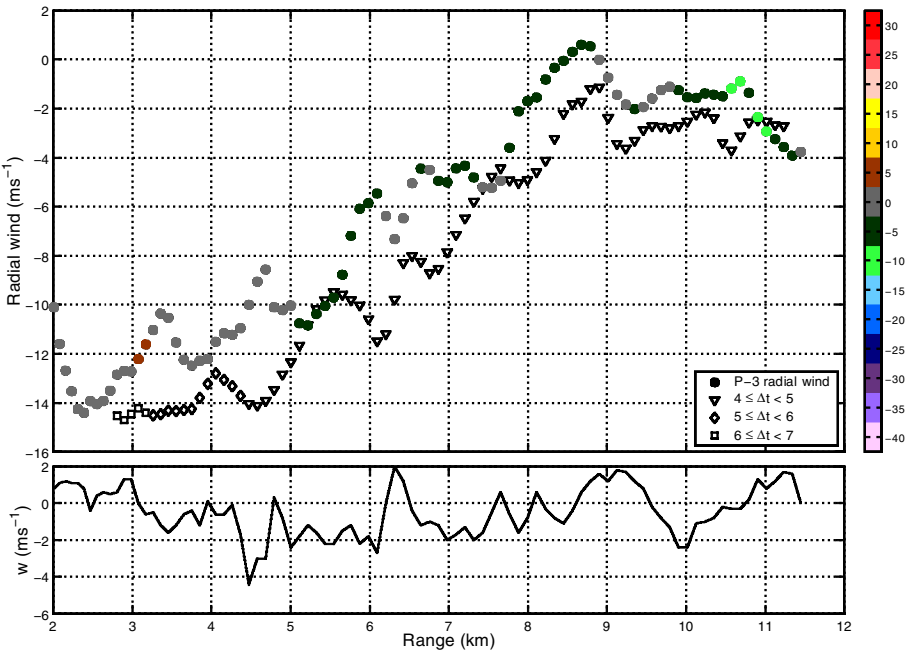

Figure 4. Comparison of radial wind speeds from P-3 data collected during the period 1251:05–1252:40 UTC on 20 October 1999 with lidar data interpolated to the same point as the P-3 observation. Both values are plotted as a function of radial distance away from the lidar along the flight leg shown in Fig. 3. Solid circles are the P-3 observations, coloured according to the scale at the right to indicate the roll angle (degrees) of the aircraft. The corresponding lidar observation is shown by a symbol that indicates the time offset (Δt, minutes) between the two observations. The vertical velocity component (w) observed by the P-3 is plotted in the lower panel.

eight lidar-retrieved wind speeds used in the tri-linear interpolation is less than 25 $m^2 s^{-2}$ (see section 4(b)).

The lidar wind speeds are plotted using a symbol that indicates the time offset between the lidar and the P-3 observations. The time offset is largest near the lidar (6 to 7 minutes) and then decreases to 4 to 5 minutes farther downstream. The variation in the time offset arises because the lidar volume scans were constructed from successive azimuthal scans, and those points nearest the lidar were sampled at somewhat higher elevation angles than those farther downwind. The colours used to plot the P-3 winds indicate the aircraft's roll angle at the time of each observation. On this flight track the P-3 remained nearly level, with roll angles between -12.5° (banked left) and 7.5° (banked right). The overall agreement between the two observations shown in Fig. 4 is quite good and does not show a significant dependence on the time offset.

Also plotted in the lower panel of Fig. 4 is the vertical velocity component observed by the P-3. The vertical velocity is dominated by short-wavelength contributions; the largest amplitude perturbation is -4 m s^{-1} and occurs approximately 4.5 km down valley from the lidar.

The next comparison is between another down-valley lidar scan collected on 30 October 1999 between 2 and 10 minutes after the 1110:40–1112:15 UTC P-3 leg through the same volume. This P-3 leg was flown at approximately 1330 m, roughly 700 m lower than the flight track considered in the previous comparison. The lidar observations of the radial wind field at 1280 m are shown by the colour-contoured fields in the right and left sections of Fig. 5. As indicated in the left section of Fig. 5,

the P-3 track was approximately level, varying between 1300 and 1340 m. The right section of Fig. 5 demonstrates that agreement between the lidar and the P-3 wind data is excellent, except for a small region near the lidar. Note that the horizontal distribution of the lidar-retrieved wind field is similar to that shown in Fig. 3, with significantly stronger winds on the east side of the valley along the flank of Patscherkofel. The presence of high winds along the Patscherkofel side of the valley during the 30 October event has also been noted in observational analyses and numerical simulations by Flamant *et al.* (2002). The total wind vector is once again directed down valley and is almost perfectly aligned with the axis of the valley, although the southernmost P-3 data point plotted in both Figs. 3 and 5 shows the wind deviating to the right of the valley axis.

A point-by-point comparison of the P-3 and linearly interpolated lidar data along this flight track appears in Fig. 6. In this case there is a wide variation in the time offset between the lidar and P-3 observations. This is because the lidar volume was constructed from successive elevation scans and the P-3 track intersected every elevation scan. The earliest scans, which have the smallest time offset, begin at the westernmost edge of the lidar volume. The P-3 also banks through a wider range of roll angles, between -22.5° and 7.5°. As apparent in Fig. 6, the radial-wind observations are in very good agreement. Despite the wide variation in the time offset along this flight leg, the difference between the two observations shows no significant dependence on that offset. As was the case in Fig. 4, the lidar-derived winds are systematically lower than those obtained from the P-3. This bias is also present in many other scans and will be discussed further in section 4(b). The vertical-velocity variations along the P-3 track are again dominated by short-wavelength signals, with one upward spike greater than 3 m s^{-1} evident about 8.7 km down valley.

The next comparison involves an up-valley lidar scan taken during the 1014:30–1017:00 UTC P-3 flight leg on 30 October 1999. The P-3 was flying at an elevation of approximately 1900 m, and as shown by the left section of Fig. 7, its track was approximately horizontal (varying between 1880 and 1920 m). The agreement between the P-3 observations and the lidar-derived winds at 1880 m, shown in the right section of Fig. 7, is good except in the region farthest upstream of the lidar, where the wind speeds obtained from the P-3 are considerably greater than those retrieved by the lidar. Also note that the total horizontal wind vector is directed somewhat to the right of the axis of the valley along much of the P-3 track, and that the lidar data show a small region of reversed flow on the west side of the valley about 6 km south of the lidar.

A point-by-point comparison between the P-3 and the linearly interpolated lidar data along this track appears in Fig. 8. No lidar-derived values are plotted at ranges between 8 and 10 km because this segment of the P-3 track lay just to the east of the volume scanned by the lidar (see Fig. 7). Once again the general agreement between the two datasets is not obviously correlated with the time offset between the observations. The agreement between both observations is rather good until about 13–14 km down valley, where the lidar observations indicate an almost calm wind while the P-3 observed radial winds of about 8 m s^{-1}. Note that in the region of maximum disagreement, the P-3 is banked to a roll angle of the order of -40°. The roll angles encountered along this up-valley flight segment, ranging between -42.5° and 17.5° (and to 32.5° just beyond the maximum up-valley range of the lidar) are considerably larger than those experienced during the two previously described down-valley legs. As will be discussed further in section 4(b), the discrepancy in the region 13–14 km up valley may be due to errors in P-3 wind observations collected at a high negative roll angle.

The vertical velocity observed by the P-3 (lower panel of Fig. 8) shows a coherent signal with an amplitude of 2 m s^{-1} and a horizontal wavelength of roughly 8 km. The

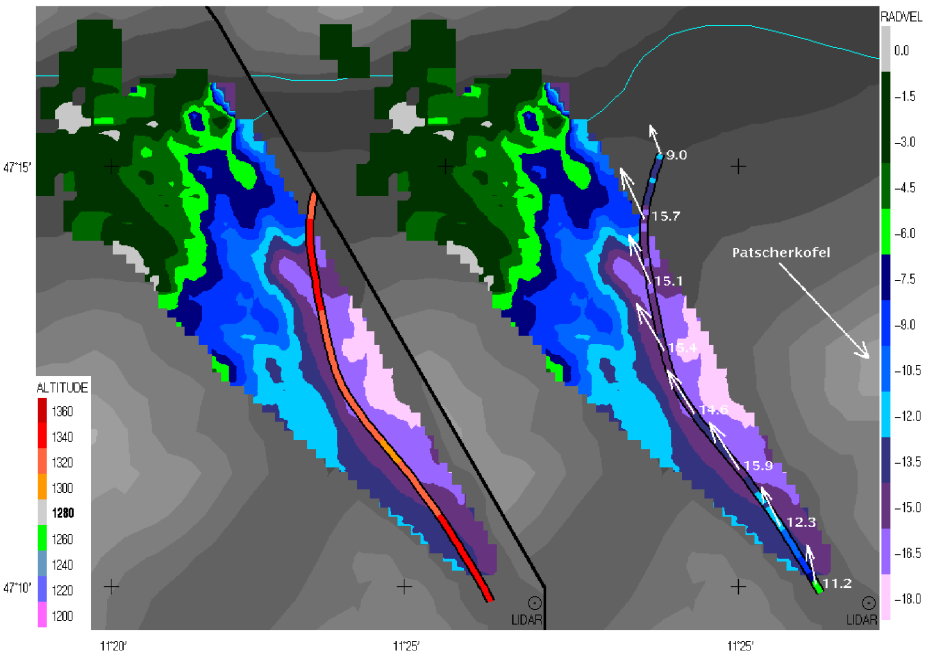

Figure 5. As in Fig. 3 except the P-3 and lidar radial wind data are compared at approximately 1111 UTC on 30 October 1999, and the lidar data are interpolated to a horizontal surface at 1280 m (above mean sea level).

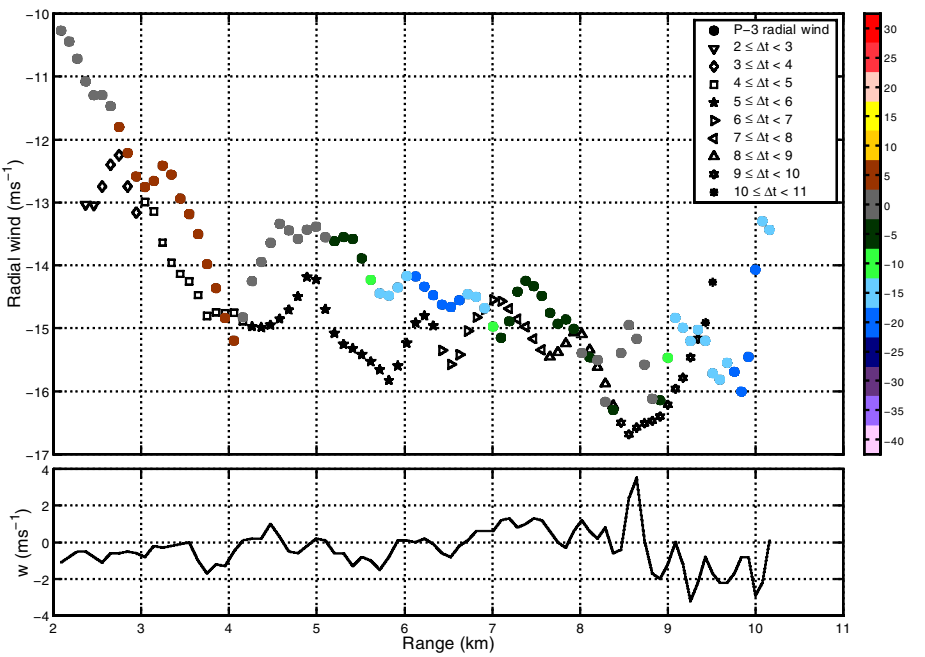

Figure 6. As in Fig. 4 except the P-3 data were collected during the period 1110:40–1112:15 UTC on 30 October 1999.

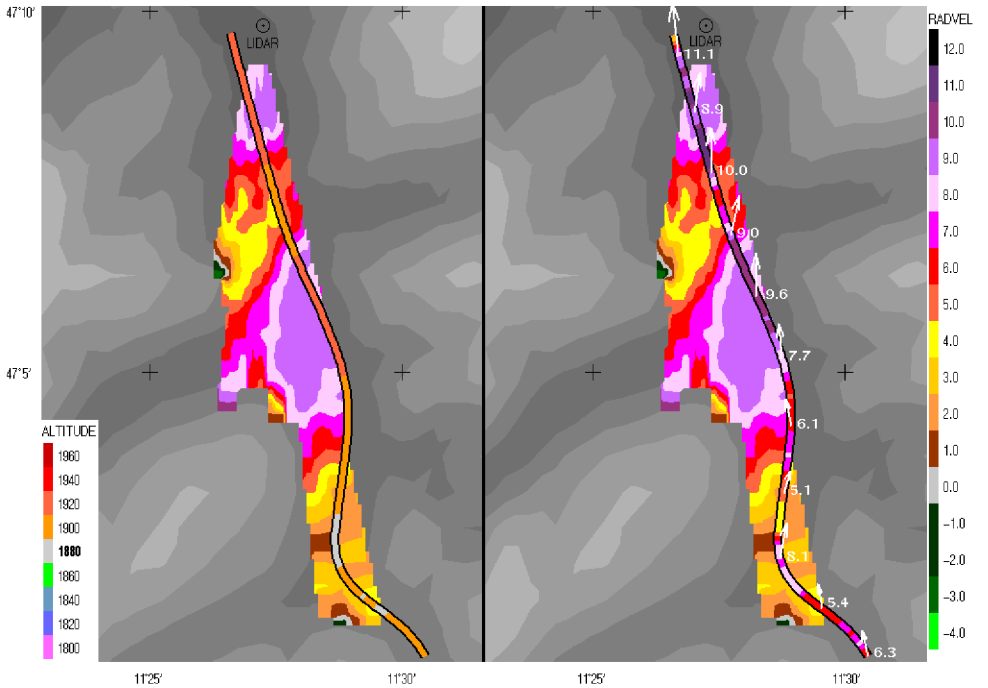

Figure 7. As in Fig. 3 except the P-3 and lidar radial wind data are compared at approximately 1015 UTC on 30 October 1999, and the lidar data are interpolated to a horizontal surface at 1880 m (above mean sea level).

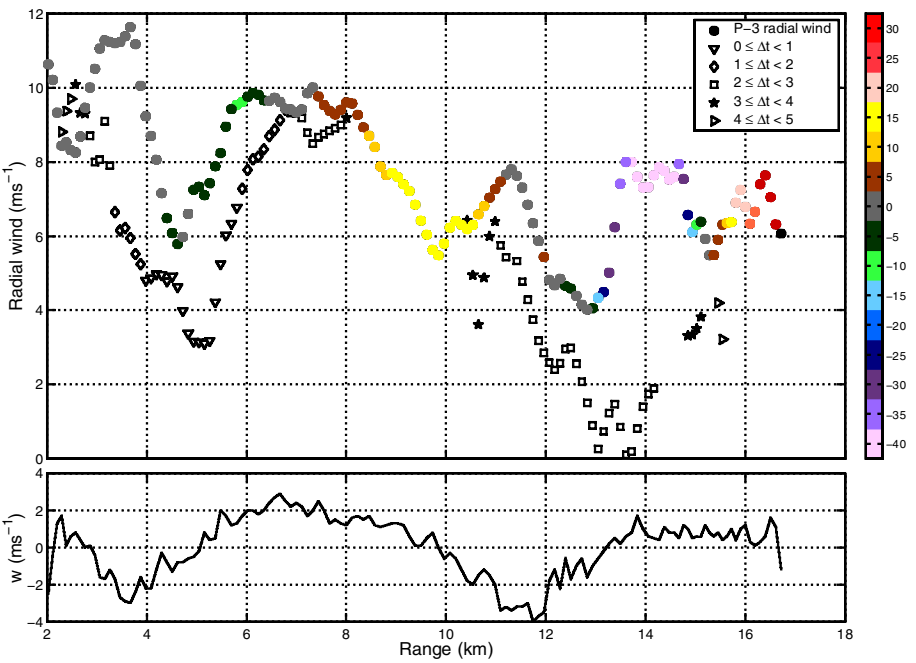

Figure 8. As in Fig. 4 except the P-3 data were collected during the period 1014:30–1017:00 UTC on 30 October 1999.

maximum downdraughts (at 3.5 and 11.5 km) are almost in quadrature with the two major radial velocity minima (at 5 and 13 km), which would be consistent with the interpretation of this feature as a trapped internal gravity wave. Note that the lidar data show the major minimum at 13 km better than the P-3 data.

The last comparison is another up-valley case taken from 30 October 1999, about 6 hours after the case shown in Figs. 7 and 8, but the level at which the data are compared is approximately 3000 m, roughly 1200 m higher than in the previous case. The P-3 traversed the lidar volume during the period 1444:30–1447:00, and as shown in the left section of Fig. 9, its altitude varied from 3010 to 3050 m. The radial winds retrieved by the lidar at 3070 m are compared with those from the P-3 in the right section of Fig. 9. In general, the agreement is rather good. In particular, both platforms document a region of dramatically reduced radial winds about 7 km south of the lidar. This region of reduced wind speed is also quite apparent in the point-by-point comparison of P-3 and linearly interpolated lidar winds shown in Fig. 10. Also apparent in Fig. 10 are regions 10, 13 and 19 km up valley, in which the lidar observations show significant patches of locally decreased winds that are not corroborated by the P-3 data. The source of these discrepancies is not known. Large positive roll angles (25°) were recorded throughout the segment between 17 and 19 km, and may be associated with the discrepancy at 19 km (although there is almost no disagreement between the lidar and P-3 observations in some portions of this same segment). The roll angles that accompany the discrepancy near 10 km are, however, almost zero, and those at 13 km are not particularly large.

Although the P3 and lidar observations 10 and 13 km up valley from the lidar are no more than 4 minutes apart, it is possible that the flow in these regions is so non-steady that the two observational platforms are sensing different microscale flows. Some indication of the potential time variations in the flow can be obtained by comparing the wind distribution in the 1445 UTC lidar volume scan with that in a second up-valley scan collected 20 minutes earlier. Such a comparison (not shown) reveals regions in the vicinity of the P-3 in which the wind speed changes by at least 4 m s^{-1} over the 20 minute period. If such flow variations occur with sufficient rapidity, they could account for many of the differences between the P-3 and lidar observations in Figs. 8 and 10.

It is also possible that the uncertainty in the horizontal position of the P-3 may contribute to the discrepancies between the P-3 and lidar velocities. The uncertainty in the horizontal position of the P-3 may be as large as 100 m, which is of the same order as the horizontal spacing between the lidar data points used in the linear interpolation Eqs. (1)–(5). Depending on whether the lidar volume is constructed from azimuthal or elevation scans, the angular distance between a pair of individual data points, such as V_{000} and V_{100} in Fig. 2, is between 1° and 1.5°; 8 km down range this angular separation is equivalent to a spatial separation of between 140 and 209 m. Attempts to empirically improve the agreement between the lidar and P-3 winds for the case shown in Fig. 10, by shifting the P-3 flight track 50 and 100 m along each of the four primary compass directions did not, however, yield a clear improvement.

The vertical velocities plotted in the lower panel in Fig. 10 show evidence of a relatively coherent signal with an amplitude of 2 m s^{-1} and a wavelength of 8 km, similar to that seen 4 hours earlier on the same day (Fig. 8). A large-amplitude short-wavelength perturbation, with extrema of -4 and 5 m s^{-1}, is also present. The nodal point ($w = 0$) in this perturbation is approximately coincident with the region of rapid horizontal flow deceleration 7 km up valley from the lidar.

It is noteworthy that the total horizontal velocity vector shown in the right section of Fig. 9 deviates substantially to the right of the along-valley axis. The westerly component to the flow shown in Fig. 9 reflects the influence of the upper-level winds,

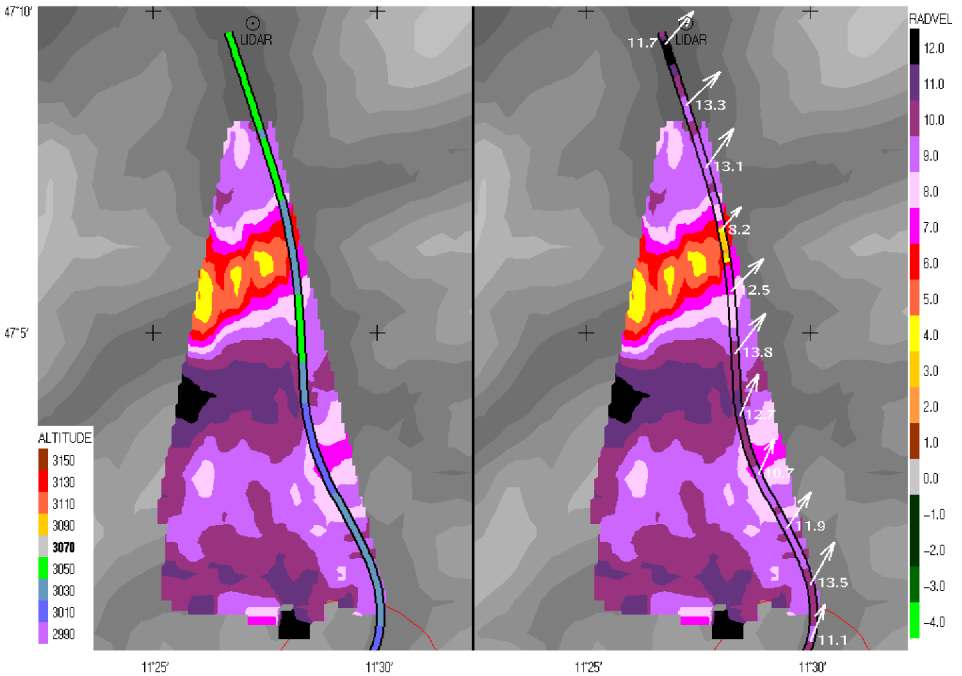

Figure 9. As in Fig. 3 except the P-3 and lidar radial wind data are compared at approximately 1445 UTC on 30 October 1999, and the lidar data are interpolated to a horizontal surface at 3070 m (above mean sea level).

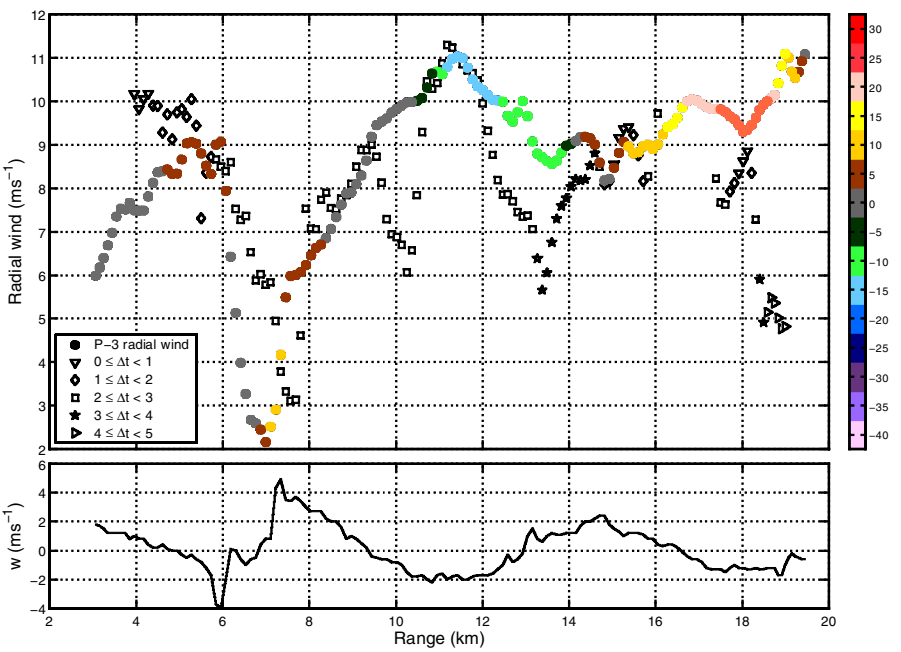

Figure 10. As in Fig. 4 except the P-3 data were collected during the period 1444:30–1447:00 UTC on 30 October 1999.

which were from the south-west. The 3 km elevation of this flight track is slightly above the 2.6–2.8 km high peaks that mark the eastern rim of the Wipptal but it is still 500 m below the highest peaks along the main east–west ridge dividing the watersheds on the northern and southern sides of the Alps.

The maximum range of the lidar varied substantially among the four cases shown in Figs. 4, 6, 8 and 10. This situation was common throughout the experiment as the distribution of aerosol scatterers in the Wipptal seemed to be quite variable. Typically, the range down valley exceeded the range up valley because the aerosol concentrations in the lower valley were enriched by emissions from the city of Innsbruck. On 30 October 1999, however, Saharan dust aerosol was present throughout the region and the down-valley range was about 10 km (Fig. 6), whereas the up-valley range varied during the day between 15 and 19 km (Figs. 8 and 10).

(*b*) *Comparison using the aggregated dataset*

There are 2203 possible point-by-point comparisons along the 24 flight tracks listed in Table 2. The r.m.s. difference between the corresponding values in the linearly interpolated lidar data and the P-3 data for the entire dataset is 3.78 m s^{-1}. The r.m.s. difference between the P-3 and lidar observations was also computed after filtering the complete dataset using various quality-control criteria. These quality-control criteria were: the backscatter (B), the signal quality index (S_{QI}), the radial distance from the lidar (r), the roll angle of the P-3 (χ), the variance among the wind speeds at the eight centroids used to interpolate the lidar winds to the location of the P-3 (σ^2), and the magnitude of the time offset ($|t_L^* - t_{P3}^*|$, where t_{P3}^* is the time of the P-3 observation at each point and t_L^* is the time of the lidar observation as interpolated to the same point). The r.m.s. differences for all data points meeting various quality-control thresholds are given in Table 3; also listed is the number of data points satisfying each particular condition.

The first three sections of Table 3 refer to parameters relevant to the quality of the lidar wind retrieval: backscatter, signal quality index, and radial distance to the point of the observation. Of the three, radial distance is clearly the least useful index in the sense that first, there is no distance threshold criterion that can be used to reduce the r.m.s. difference below 3 m s^{-1} and second, those threshold distances that yield relatively small r.m.s. differences (such as $r \leqslant 8$ km) require one to discard over half of the potentially available data. The other two indices have better quality-control potential and appear to give similar results, although the signal quality index is slightly more discriminating than the backscatter. For example, comparing the effectiveness of two alternative criteria $B \geqslant 28$ dB and $S_{QI} \geqslant 80$, it may be observed that the condition $S_{QI} \geqslant 80$ yields a slightly smaller r.m.s. difference between the P-3 and lidar observations than the condition $B \geqslant 28$ dB (2.97 versus 2.98 m s^{-1}) but still allows more points to satisfy the threshold criterion (1687 versus 1593).

The next section in Table 3 refers to controls on the quality of the P-3 wind data. The P-3 wind observations are believed to be more sensitive to roll angle than to most other raw data inputs (Merceret 1982), but if the r.m.s. difference between the P-3 and lidar winds is tabulated as a function of the magnitude of the roll angle, no sensitivity to the magnitude of the roll angle is evident. The sensitivity to roll angle is, however, not necessarily symmetric. A. Barry Damiano (personal communication) has suggested that the placement of the angle-of-attack pressure probe on the left side of the P-3 fuselage may shield the instrument during left turns and reduce the accuracy of the velocity measurements when the P-3 is at a steep negative roll angle. Thus, rather than tabulate

TABLE 3. COMPARISON OF THE R.M.S. DIFFERENCES BETWEEN THE P-3 AND LIDAR RADIAL WIND OBSERVATIONS, WHEN THE DATA IS FILTERED TO SATISFY VARIOUS QUALITY-CONTROL PARAMETERS

Threshold criterion	r.m.s. difference ($m\ s^{-1}$)	Number of points
	Backscatter (dB)	
$B \geqslant 25$	3.69	2097
$B \geqslant 26$	3.38	1943
$B \geqslant 28$	2.98	1593
$B \geqslant 30$	2.90	1304
	Signal quality index	
$S_{QI} \geqslant 50$	3.37	2007
$S_{QI} \geqslant 60$	3.14	1883
$S_{QI} \geqslant 80$	2.97	1687
$S_{QI} \geqslant 120$	2.87	1351
	Radial distance (km)	
$r \leqslant 15$	3.52	1927
$r \leqslant 10$	3.45	1371
$r \leqslant 8$	3.17	1008
$r \leqslant 6$	3.12	603
$r \leqslant 4$	3.30	222
	Roll angle (degrees)	
$-50 \leqslant \chi < -30$	6.83	60
$-30 \leqslant \chi < -15$	5.18	126
$-15 \leqslant \chi < -5$	4.07	183
$-5 \leqslant \chi < 0$	3.69	522
$5 \geqslant \chi > 0$	3.32	706
$15 \geqslant \chi > 5$	3.09	408
$30 \geqslant \chi > 15$	3.88	151
$50 \geqslant \chi > 30$	5.57	26
	Variance ($m^2 s^{-2}$)	
$\sigma^2 \leqslant 144$	3.14	2041
$\sigma^2 \leqslant 25$	2.97	1958
$\sigma^2 \leqslant 6$	2.81	1706
$\sigma^2 \leqslant 4$	2.77	1536
	Time offset (minutes)	
$\lvert t_L^* - t_{P3}^* \rvert \leqslant 10$	3.61	2068
$\lvert t_L^* - t_{P3}^* \rvert \leqslant 9$	3.54	1935
$\lvert t_L^* - t_{P3}^* \rvert \leqslant 7$	3.39	1610
$\lvert t_L^* - t_{P3}^* \rvert \leqslant 5$	2.91	1018
$\lvert t_L^* - t_{P3}^* \rvert \leqslant 4$	2.80	808

The right column gives the number of data points that satisfy each quality-control condition.

threshold filtering criteria based on the magnitude of the roll angle, the data were binned as a function of positive and negative roll angles and the r.m.s. differences for those bins are listed in Table 3. The asymmetry of the distribution of the r.m.s. differences as a function of roll angle is striking. The smallest differences were achieved with positive roll angles between 5° and 15 °. Negative roll angles in the range −15° to −5° gave worse agreement than steeper positive roll angles in the range 15° to 30°. The r.m.s. differences were very large for P-3 data collected at negative roll angles steeper than −15°.

Not shown in the table is the r.m.s. difference for the 21 observations collected when the P-3 reported zero roll angle. The r.m.s. difference for these observations, 4.22 $m\ s^{-1}$, is actually rather large, but due to the small sample size and the fact that much better results were obtained from the 1128 data points involving roll angles with magnitudes

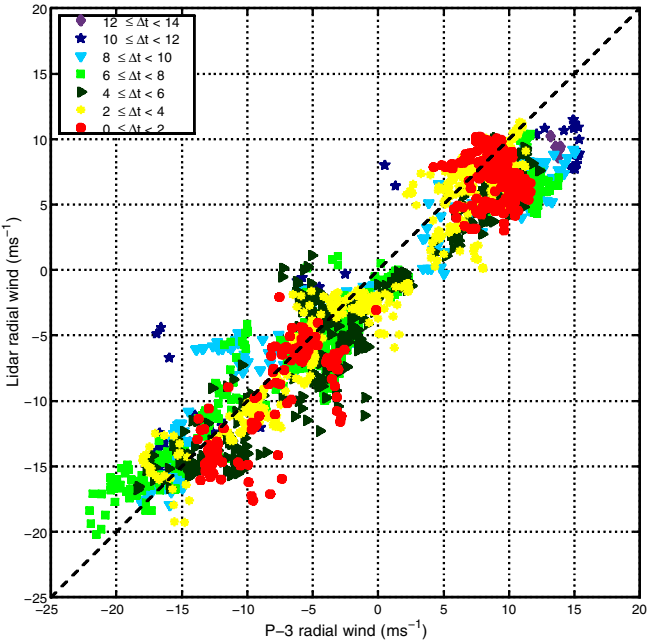

Figure 11. Scatter plot of P-3 versus lidar-retrieved radial winds for all data for which the variance $\sigma^2 \leqslant 25\ \mathrm{m^2 s^{-2}}$. The time offset Δt) for each data point is indicated by the colour and shape of each symbol.

between 0 and 5°, the large r.m.s. errors for the zero-roll-angle observations do not appear to be statistically significant.

Although roll angle does seem to be a significant factor in the r.m.s. difference between the P-3 and lidar wind observations, it is not possible to design a particularly effective filter criterion based on roll angle alone. Most roll-angle thresholds allow relatively large r.m.s. errors. The best agreement could be obtained by imposing the non-intuitive criterion that $15 \geqslant \chi > 5$, which reduces the r.m.s. error below 3.1 m s^{-1} but requires one to discard 81% of the data.

The final two sections of Table 3 refer to parameters that relate to the probability that the P-3 and lidar observations should actually be identical: (i) the time offset between the two observations and (ii) the variance of the lidar-retrieved winds among the eight points surrounding the P-3 observations, which is a measure of the spatial homogeneity of the flow. The best agreement between datasets is achieved using cut-off criterion based on the variance. Note in particular that the filtering criterion $\sigma^2 \leqslant 25\ \mathrm{m^2 s^{-2}}$ yields an r.m.s. difference of less than 3 m s^{-1} while still being satisfied by 1958 (89%) of the observations. It is hardly surprising that there is better agreement between a point-wise measurement and measurements averaged over a volume in circumstances where the wind field exhibits more spatial homogeneity. One might suppose that the agreement would be similarly sensitive to the time offset, but there is not much change in the r.m.s. difference until $|t^*_{\mathrm{L}} - t^*_{\mathrm{P3}}|$ drops below 5 minutes, a relatively restrictive condition that is only satisfied by 1018 (46%) of the dataset.

A final comparison between the two datasets is provided in Fig. 11 which is a scatter plot of the P-3 radial wind against the lidar-retrieved radial wind for all data points satisfying the condition $\sigma^2 \leqslant 25\ \mathrm{m^2 s^{-2}}$. The time offset is indicated by the shape and colour of each symbol, with warm colours representing small offsets. The agreement

TABLE 4. CONTRAST BETWEEN UP-VALLEY AND DOWN-VALLEY MEAN AND R.M.S. VALUES OF SIGNIFICANT PARAMETERS FOR DATA POINTS IN WHICH THE VARIANCE $\sigma^2 \leqslant 25\ \mathrm{m^2 s^{-2}}$

Parameter	Up valley	Down valley	Combined total
Number of points	735	1223	1958
r.m.s. difference (m $\mathrm{s^{-1}}$)	3.38	2.69	2.97
Mean difference (P3−lidar, m $\mathrm{s^{-1}}$)	2.42	0.41	1.16
r.m.s. roll angle (°)	12.0	10.3	10.9
Mean roll angle (°)	1.6	1.3	1.4
30 October 1999 only			
Mean radial wind (P3, m $\mathrm{s^{-1}}$)	9.17	7.62	
Mean radial wind (lidar, m $\mathrm{s^{-1}}$)	6.75	8.35	

between the two data sources does not exhibit an obvious dependence on the time offset. On the other hand, there is an obvious bias in which the lidar-retrieved positive radial winds (winds blowing toward the lidar from the direction of the Brenner Pass) are smaller than the values collected by the P-3. No large bias is evident, however, in the comparisons involving observations collected when the lidar was pointed down the valley toward Innsbruck.

A closer look at the differences between the up-valley and down-valley results is provided in Table 4. The down-valley comparisons, which were possible on three different days, are more numerous than the up-valley comparisons, which were only available on 30 October. The r.m.s. differences and the bias are larger up valley than down valley, but there is a much bigger difference in bias. The value of the P-3 wind minus the lidar wind is 2.4 m $\mathrm{s^{-1}}$ up valley and only 0.4 m $\mathrm{s^{-1}}$ down valley. The source of this difference is unclear. It may be at least partly due to increased errors in the P-3 observations due to more rapid and steeper rolling in the narrower upper portion of the Wipptal, which is consistent with the finding that the r.m.s. roll angle is greater up valley. Nevertheless, the mean roll angles are both positive and similar up and down valley. The distribution of data points with large negative roll angles, and therefore potentially larger r.m.s. differences (not shown), is also similar up and down valley. Alternatively, it is possible that the flow up valley was inherently less stationary making it harder for the P-3 and the lidar to actually sample the same microscale structures.

Dabas *et al.* (1998) identified uncorrected chirp as a possible source of bias in Doppler-lidar measurements. The signal processing algorithm discussed in section 2(b) should eliminate most of the chirp-induced bias in these observations. Furthermore, chirp-induced errors do not appear capable of producing the large difference in the bias between the up- and down-valley measurements. Thus, we do not believe chirp is likely to be the source of the bias evident in Table 4.

One of the most unsettling aspects of the comparison between the P-3 and lidar radial wind data is revealed by the last two lines in Table 4, which compare the mean winds sampled by each instrument during a single event. On the basis of the P-3 data alone, one would conclude that the gap flow in the Wipptal experienced an average *deceleration* of 1.5 m $\mathrm{s^{-1}}$ between the up-valley and down-valley sampling volumes. On the other hand, the lidar data suggests an average *acceleration* of 1.6 m $\mathrm{s^{-1}}$ occurred between the same regions. One of the theoretical challenges MAP was designed to address was to better understand the factors that contribute to flow acceleration in mountain gaps. On 30 October 1999 the P-3 and lidar data are in conflict as to whether the time- and volume-averaged flow experienced acceleration or deceleration between the upper and lower parts of the valley. Data from three dropsondes, which were released

into the Wipptal between 0920 and 0922 UTC, support the idea of an average flow acceleration, although the dropsondes were not sampling precisely the same regions or at the same times as the P-3 and the lidar.

5. Conclusions

The radial wind component observed by the NOAA/ETL scanning Doppler lidar was compared with the same component of the horizontal winds measured *in situ* by the NOAA P-3 on three days during the MAP Special Observing Period when the two instruments collected data almost simultaneously. Point-by-point comparisons were conducted by tri-linearly interpolating the raw lidar data to the same points at which the P-3 measurements were conducted.

Comparisons were presented along four individual P-3 flight tracks. Depictions of the spatial variations along each flight track superimposed on contour plots of the lidar-retrieved winds at the same level demonstrate that the two instruments generally record the same variations in flow structure. The similarity of the lidar and *in situ* wind observations was confirmed by more quantitative point-by-point comparisons along each flight track. The along-track comparisons also suggested a systematic tendency for the P-3 observations to yield slightly higher wind speeds than those obtained from the lidar data. In addition, isolated regions appear in the up-valley scans in which the lidar winds were much weaker than those recorded by the P-3.

The tendency for the P-3 radial winds to exceed those in the lidar data was also apparent in the analysis of the aggregated dataset (see Fig. 11). The aggregated dataset was used to investigate several potential quality-control parameters that might be employed to filter the data and reduce the r.m.s. difference between the measurements collected by each platform. Useful filters for the lidar data itself include the backscatter and the signal quality index, both of which could be set to reduce the r.m.s. difference to 3 m s^{-1} without discarding more than roughly one quarter of the observations. The r.m.s. difference between the P-3 and lidar data was also sensitive to the roll angle of the P-3, but it was difficult to specify a filtering criterion on the basis of roll angle alone that would give r.m.s. differences close to 3 m s^{-1} without eliminating 80% of the data.

The most discriminating filter involved a parameter that indicates how likely the point measurement from the P-3 is to agree with the volume-averaged sample retrieved by the lidar. That parameter is the variance σ^2 among the eight raw lidar data points that are tri-linearly interpolated to the spatial location of the P-3 observation. The smallest r.m.s. difference (less than 2.77 m s^{-1}) was obtained when this variance was small (less than 4 m^2 s^{-2}). Similarly small r.m.s. differences can also be obtained using only those points for which the time offset between the two observations was smaller than 4 minutes, but this is a rather restrictive condition that requires discarding more than half the raw data, and the resulting r.m.s. difference is still larger than that obtained by enforcing less restrictive conditions on the variance (see Table 3).

The overall quality-controlled ($\sigma^2 \leqslant 25$ $m^2 s^{-2}$) r.m.s. difference between radial wind speeds measured by each platform was 3.0 m s^{-1}, with larger r.m.s. errors in the region up valley from the lidar than in the region down valley. This is twice the 1.5 m s^{-1} r.m.s. difference between lidar observations and rawindsondes obtained by Hall *et al.* (1984). The Hall *et al.* (1984) observations were not, however, 'point-wise' comparisons in a highly non-homogeneous flow, such as that in the Wipptal; instead the lidar collected data from conical scans in a horizontally uniform environment and the horizontal velocity at each level was determined by a 'best-fit' sinusoidal curve.

A bias was also evident, in which the wind speeds from the P-3 exceeded those from the lidar. This bias was small down valley (0.4 m s^{-1}) and much larger up valley (2.4 m s^{-1}). The source of this basis has not been definitely established but it may be due to the tendency of the P-3 to bank more steeply and more rapidly in the narrow upper portion of the Wipptal, thereby degrading the accuracy of its wind observations. It may also be that the winds were more non-steady in the upper portion of the Wipptal, making it more difficult for the P-3 and the lidar to actually observe the same microscale flow.

Considering the substantial differences in the instrumentation and the sampling strategies used by P-3 and lidar, the overall agreement between the two datasets is very good down valley and satisfactory up valley. It appears that these two data sources can be intelligently combined to give accurate composite analyses of the airflow in the Wipptal. This investigation also suggests quantitative values that might be used to implement automated quality controls on the Doppler-lidar data collected in the Wipptal during MAP. Reasonable quality control could be achieved by thresholding out those values with signal quality indices less than 80, or backscatter values less than 28 dB.

Acknowledgements

The authors gratefully acknowledge many helpful conversations with A. Barry Damiano and Barry Rye. Stacy Brodzik provided invaluable assistance with the MountainZebra software. Durran and Maric's participation in this research was sponsored by National Science Foundation grants ATM-9817728 and ATM-0137335. Banta, Hardesty and Darby's participation, was funded by the NOAA Environmental Research Laboratory and Office of Atmospheric Research.

References

Banta, R. M., Olivier, L. D., Holloway, E. T., Kropfli, R. A., Bartram, B. W., Cupp, R. E. and Post, M. J. 1992 Smoke column observations from two forest fires using Doppler lidar and Doppler radar. *J. Appl. Meteorol.*, **31,** 1328–1349

Banta, R. M., Darby, L. S., Kaufmann, P., Levinson, D. H. and Zhu, C.-J. 1999 Wind-flow patterns in the Grand Canyon as revealed by Doppler lidar. *J. Appl. Meteorol.*, **38,** 1069–1083

Bougeault, P., Binder, P., Buzzi, A., Dirks, R., Houze, R., Kuettner, J., Smith, R. B., Steinacker, R. and Volkert, H. 2001 The MAP Special Observing Period. *Bull. Am. Meteorol. Soc.*, **82,** 433–462

Corbet, J., Mueller, C., Burghart, C., Gould, K. and Granger, G. 1994 Zeb: Software for integration, display, and management of diverse environmental datasets. *Bull. Am. Meteorol. Soc.*, **75,** 783–792

Dabas, A. M., Drobinski, P. and Flamant, P. H. 1998 Chirp-induced bias in velocity measurements by a coherent Doppler CO_2 lidar. *J. Atmos. Oceanic Technol.*, **15,** 407–415

Flamant, C., Drobinski, P., Nance, L., Banta, R., Darby, L., Dusek, J., Hardesty, M., Pelon, J. and Richard, E. 2002 Gap flow in an Alpine valley during a shallow south föhn event: Observations, numerical simulations, and hydraulic analogue. *Q. J. R. Meteorol. Soc.*, **128,** 1173–1210

Hall Jr, F. F., Huffaker, R. M., Hardesty, R. M., Jackson, M. E., Lawrence, T. R., Post, M. J., Richter, R. A. and Weber, B. F. 1984 Wind measurement accuracy of the NOAA pulsed infrared Doppler lidar. *Appl. Optics*, **23,** 2503–2506

James, C., Brodzik, S., Edmon, H., Houze Jr, R. A. and Yuter, S. E. 2000 Radar data processing and visualization over complex terrain. *Weather and Forecasting*, **15,** 327–338

Merceret, F. J. 1982 'The sensitivity of variables computed from RFC WP3D flight data to fluctuations in the raw data inputs'. NOAA Technical Memorandum ERL RFC-8

Post, M. J. 1978 Experimental measurements of atmospheric aerosol inhomogeneities. *Optics Lett.*, **2,** 166–168

Post, M. J. and Cupp, R. E. 1990 Optimizing a pulsed Doppler lidar. *Appl. Optics*, **29,** 4145–4158

Rye, B. J. and Hardesty, R. M. 1993 Discrete spectral peak estimation in incoherent backscatter heterodyne lidar. II: Correlogram accumulation. *IEEE Trans. Geosci. Remote Sens.*, **31,** 28–35